FISEVIER

Contents lists available at ScienceDirect

Acta Materialia

journal homepage: www.elsevier.com/locate/actamat



Full length article

Origins of strengthening and failure in twinned Au nanowires: Insights from in-situ experiments and atomistic simulations



Zhuocheng Xie^a, Jungho Shin^{b,c}, Jakob Renner^{a,d}, Aruna Prakash^{a,e}, Daniel S. Gianola^b, Erik Bitzek^{*,a}

- a Friedrich-Alexander-Universität Erlangen-Nürnberg, Materials Science & Engineering, Institute I, Martensstr. 5, Erlangen 91058, Germany
- ^b Materials Department, Santa Barbara, University of California Santa Barbara, California 93106, USA
- ^c CNRS, IM2NP, Aix Marseille Univ, Université de Toulon, Marseille, France
- d Friedrich-Alexander-Universität Erlangen-Nürnberg, Materials Science & Engineering, Chair of Materials Science and Engineering for Metals, Martensstr. 5, Erlangen 91058. Germany
- ^e Technische Universität Bergakademie Freiberg, Institute of Mechanics and Fluid Dynamics, Micromechanical Materials Modelling, Lampadiusstr. 4, Freiberg 09599, Germany

ARTICLE INFO

Article History: Received 14 June 2019 Revised 9 January 2020 Accepted 20 January 2020 Available online 23 January 2020

Keywords:
Nanowire
Coherent twin boundary
Plasticity
In-situ tension test
Molecular dynamics

ABSTRACT

The deformation behavior of (110)-oriented twinned Au nanowires (NWs) with multiple longitudinal coherent twin boundaries (CTBs) under tension is studied using in-situ experiments and molecular dynamics (MD) simulations. The twinned NWs show higher yield strength than the single-crystalline NWs with similar diameter. Postmortem observations using electron microscopy and MD simulations show that the presence of CTBs transitions the governing mechanism from twinning-mediated deformation in single-crystalline NWs to strongly localized deformation. MD simulations reveal that the intersection of deposited partial dislocations at the CTB with the free surfaces plays an important role in the transmission of the dislocation, leading to the formation of full dislocations instead of partial dislocations and twinning in the case of single-crystalline NWs. The repeated activation of full dislocation slip leading to localized deformation is furthermore dependent on the relative orientation of surface facets to the activated Burgers vectors. The results of this work enhance the understanding of deformation mechanisms of twinned nano-objects and suggest design strategies for mechanical systems at the nanoscale.

© 2020 Acta Materialia Inc. Published by Elsevier Ltd. This is an open access article under the CC BY license.

(http://creativecommons.org/licenses/by/4.0/)

1. Introduction

Metallic nanowires (NWs) are regarded as promising building blocks for flexible and stretchable electronic devices due to their high conductivity and optical transmittance [1–3] and often display superior mechanical properties compared to their bulk counterparts [4–10]. NWs show extremely high yield strengths close to their theoretical value, since the plasticity of these defect-free samples requires the nucleation of dislocations at the free surfaces [6,8,11]. The deformation mechanisms of face-centered cubic (FCC) single crystalline NWs (SCNWs) have been extensively studied in experiments [11–13] and molecular dynamics (MD) simulations [12–26] under different loading conditions. Pseudoelasticity and shape memory effects resulting from phase transformation or deformation twinning [14–17] and slip by full dislocations [13,18,19] were observed in MD simulations of FCC SCNWs under uniaxial deformation conditions. These simulations show

orientation and loading direction dependence of the operative deformation mechanisms in FCC SCNWs which can be explained and predicted by the generalized stacking fault energies and considering the Schmid factors for leading and trailing partial dislocations [8,12,13,23]. SCNWs under complex loading conditions, such as torsion [21,22,26] or bending [20,24,25], were also studied using MD simulations. Under bending loads, (110)-oriented SCNWs showed the formation of geometrically necessary wedge-shaped twins in the tensile part of the SCNW and full dislocations in the compressive part, and - depending on the bending direction - pesudoelasticity after load removal [24].

Similarly to NWs, nanotwinned metals have also lately attracted increasing interest because they combine high strength with high ductility, two properties which are commonly regarded as mutually exclusive [27–29]. The interactions between gliding dislocations and twins at twin boundaries increase the strength and ductility of nanocrystalline materials [27–29]. Particularly for bulk FCC metals the mechanisms of dislocation-coherent twin boundary (CTB) interactions have been studied in detail [30–34]. There, MD simulations suggest that the interactions between perfect screw as well as non-screw dislocations and CTBs

^{*} Corresponding author.

E-mail address: erik,bitzek@fau.de (E. Bitzek).

are controlled by the energy barriers for the formation of partial dislocations from the reactive sites at the CTB [30,31].

Modern materials synthesis techniques have enabled the fabrication of twinned NWs (TNWs) with different arrangements of CTBs [35–45]. Experimental studies on the mechanical properties of (110)-oriented five-fold Ag TNWs with longitudinal CTBs were reported in [35-38]. The in-situ experiments show that the preexisting CTBs give rise to pronounced strain-hardening by impeding the transmission of the surface nucleated dislocations, [46,47]. The MD simulations on five-fold TNWs show that the existence of CTBs leads to higher yield strength and more brittle plastic deformation compared with single crystalline counterparts [48–50]. (111)-oriented NWs with varying densities of twin boundaries perpendicular to the wire axis were obtained by chemical synthesis [39-43]. Similar to five-fold TNWs, these (111)-oriented TNWs show higher strength than twin-free counterparts with equivalent diameters and orientations according to the results of in-situ experiments and MD simulations [43,51,52]. With decreasing CTB spacing, the (111)-oriented TNWs show increasing yield strength [51,52] and a ductile-tobrittle transition [43]. The deformation behavior of NWs with other planar defects such as grain boundaries (GBs) [53-55] and incoherent twin boundaries (ITBs) [56] were also studied using MD simulations. The MD simulation results suggest that dislocations prefer to nucleate from triple junctions of GBs and kink-steps of ITBs due to the stress concentration of these internal defects.

Recently, the deformation behavior of (110)-oriented Au NWs with a single longitudinal CTB under tension, although without load measurements, was studied [44]. Storage of full dislocations was observed in the deformed TNWs via transmission electron microscopy (TEM). A proposed scenario is that the trailing partial dislocations may nucleate and combine with the leading partial dislocations to form full dislocations [44]. Although the dislocation reactions at CTB are well established in bulk FCC metals [30–34], the mechanism of dislocation-CTB interactions in confined dimensions where the CTB is bounded by free surfaces, forming effectively a triple junction, is still not yet well understood. More importantly, no strengthening effect was reported in the experiments, although the presence of the CTB is believed to hinder the propagation of the leading partial dislocations [44]. Microcompression experiments on (110)-oriented single crystalline and twinned bi-crystalline micro-pillars with a longitudinal CTB show similarly no significant strengthening effect of CTBs [57–59]. In these micro-scale studies, several scenarios have been proposed to explain such behavior according to the pre-existing dislocation sources and orientation of the CTBs. However, the influence of the longitudinal CTB on strength of defect-free NWs is still not understood. Whether the longitudinal CTB is able to strengthen (110)-oriented NW by impeding the motion of dislocations is an essential question to be answered.

In this work, quantitative in-situ tensile tests were performed on (110)-oriented Au multi-twinned NWs (MTNWs) in a scanning electron microscope (SEM). The experimental results are compared with previous experiments on (110)-oriented SCNWs [12] and corroborated by MD simulations to investigate the origins of the strengthening effect of CTBs. The deformation behaviors of (110)-oriented bicrystalline twinned NWs (BTNWs) and experimentally-inspired MTNWs with longitudinal CTBs under tension are investigated by performing MD simulations. The mechanisms of dislocation-CTB interactions at different applied stress and strain states are analyzed in detail and elucidated.

2. Methods

2.1. Experimental procedure

(110) oriented Au NWs containing axial twin boundaries were grown on carbon coated tungsten substrates via physical vapor

deposition under molecular beam epitaxy settings, following the identical growth procedures reported in [12,60]. A Kleindiek nanomanipulation system and a Pt-based gas injection system (GIS) with electron beam induced deposition (EBID) was utilized to transfer the Au NWs. A MTNW with a diameter of 49 nm and a length greater than 40 μm was harvested from the substrate and transferred to a TEM half grid in a cantilevered geometry following the procedure of Murphy et al. [61]. During the affixation to the half grid, the MTNW was cut in half (\sim 20 μ m), leading to two MTNWs that share the identical twin structure (same locations of TBs and orientations of twins). The divided MTNWs were characterized by TEM (JEOL 2010F) with an acceleration voltage of 200 keV observed along the $[10\overline{1}]$ zone axis (see Fig. 1a). The TEM characterization confirmed that the identical twin structure of the MTNWs contained a multiplicity of $(1\overline{1}1)$ twin planes along the whole wire length. TEM diffraction patterns along $[10\overline{1}]$ zone axes show a characteristic FCC twin pattern (inset of Fig. 1a), as corroborated by the angle measurement of 15.8° between the (111), in the twin (t) orientation and the $(0\overline{2}0)_n$ plane in the parent (p) orientation. No pre-existing dislocations were

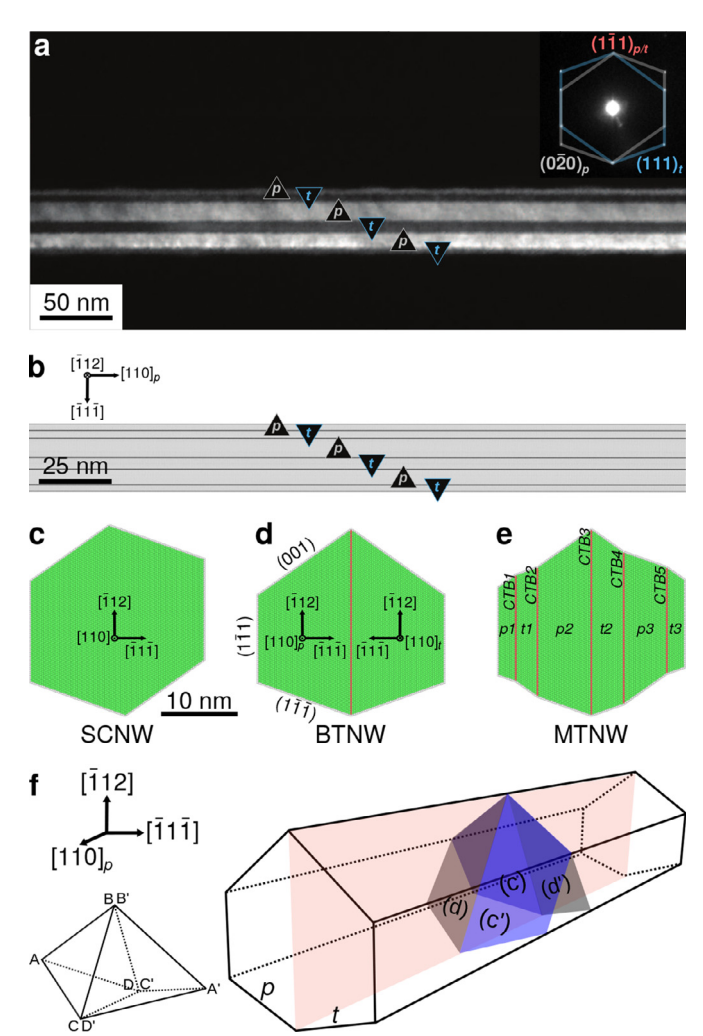


Fig. 1. a TEM dark-field image of MTNW before tensile test. p and t denote parent and twinned grains, respectively. The inset shows the corresponding selected area diffraction pattern of the MTNW. **b** Atomistic model of the MTNW along [$\overline{1}$ 12] viewing direction. Only outer-layer atoms and atoms that make up the CTB are shown here. Outer-layer atoms are half transparent. $\mathbf{c} - \mathbf{e}$ Cross-sections of the simulated NWs in this work. Atoms are colored according to CNA, where green and red colors represent atoms in FCC- and HCP-structure, respectively; white atoms are outer-layer atoms. \mathbf{f} Schematic illustration of the double Thompson tetrahedron showing the slip system in BTNWs. Red plane is the CTB, blue planes are the slip planes (c) and (c), grey planes are the slip planes (d) and (d) (For interpretation of the references to color in this figure legend, the reader is referred to the web version of this article.).

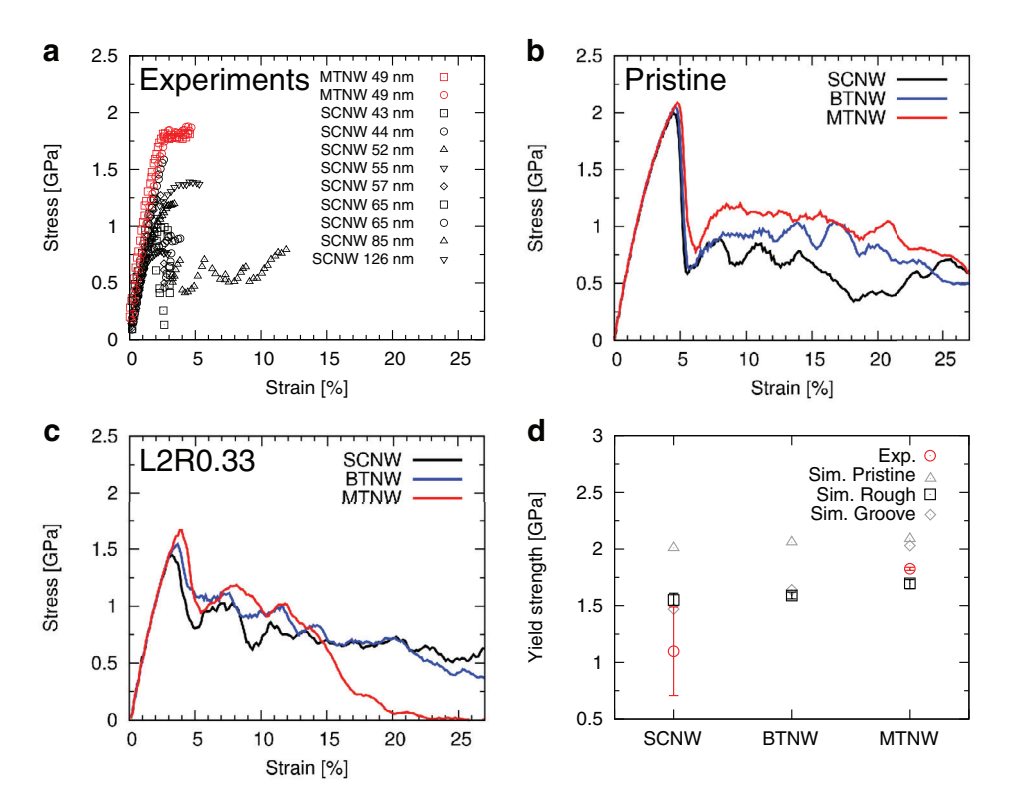


Fig. 2. a Engineering stress-strain curves of in-situ tensile tests on SCNWs [12] and MTNWs with different diameters as indicated in the legend. Engineering stress-strain curves of the simulated NWs with **b** pristine and **c** rough surfaces generated by randomly removing 33% of atoms from the two outermost layers (L2R0.33, d=24.5 nm, l=107.3 nm, T=300 K, $\dot{\epsilon} = 2 \times 10^8 \, \text{s}^{-1}$). **d** Summary of the yield strengths of the experimentally tested and simulated NWs. The yield strength values for the SCNWs include data from [12,74].

observed, as confirmed by both diffraction-contrast and high-resolution TEM of several NWs (see Figs. S1-2 in the Supplementary Material). We used these experimentally observed multi-twinned NWs to inform the MTNW simulation case study. The *in* – *situ* tensile testing system consisted of a nanopositioning stage (SmarAct GmbH), a linear piezoelectric actuator (Physik Instrumente) and a microelectromechanical systems (MEMS)-based capacitive load cell (FemtoTools), which all were installed in a SEM. The half grid with the MTNWs was mounted to the actuator side, and the final fixation for gripping of the specimen was achieved after alignment of the load cell and the MTNW using the nanopositioning stage described in [62]. A nominal strain rate of 5 \times 10⁻⁴ s⁻¹ was applied during the tensile test while simultaneous imaging was performed in a SEM. The SEM images were used for digital image correlation (DIC) to determine the specimen tensile strain. TEM analysis was also performed after the in-situ tensile tests. The details of the procedure (Fig. S3) and additional TEM micrographs of as-transferred MTNWs (Figs. S1-2) can be found in the Supplementary Material.

2.2. Simulation set-up

MD simulations were performed on [110]-oriented NWs, as shown in Fig. 1b—e. The SCNW with a hexagonal-shaped cross-section (Fig. 1c) was constructed based on experimental cross-sections of Au SCNWs [60]. The BTNW with a symmetric hexagonal-shaped cross-section (Fig. 1d) was built based on the cross-section of the hexagonal-shaped SCNW. The parent grain p has the same crystallographic orientation as the SCNW, and the twinned grain t is mirror symmetric to p with the CTB being the mirror plane. The MTNW was constructed based on the size of each twin segment determined in the experimental sample (Fig. 1b,e). Periodic boundary conditions (PBC) were applied along the wire axis. Pristine, rough and grooved surfaces were modeled in all wires, see Fig. S4 in the Supplementary Material. Rough wires were created by randomly removing a certain

percentage of atoms from the outer layers. In the following, we will use LhRx as shorthand for wires in which a fraction of x atoms has been removed from the h outermost layers. E.g., L2R0.33 indicates that one-third of atoms in the two outermost layers were randomly removed. Grooved surfaces were created by removing a single row of atoms along the $[\overline{1}01]$ orientation on a $(1\overline{1}1)$ facet in a p grain. The lengths of the grooves in SCNW and TNWs are 15.3 nm and 13.3 nm, respectively. The diameter d of the tested wires was 24.5 nm (scaled down by a factor of two from the experimental sample) and the aspect ratio (length to diameter ratio l/d) was 4.4. NWs with different diameters (d=11.3 nm, 17.4 nm, 32.0 nm and 40.0 nm) and aspect ratios (d=11.3 nm and l/d=4.4, 8.8, 17.9, 35.2 and 70.5) were also simulated. All simulated NWs in this work are summarized in Table 1 in the Supplementary Material.

The atomic interactions were modeled by an embedded-atommethod (EAM) potential for Au by Foiles [63]. Additional simulations were also performed using Cu [64] and Ag [65] EAM potentials. All pristine wires were relaxed using the FIRE algorithm [66]. The wires with rough surfaces were equilibrated at 600 K for 10 ps and then quenched by FIRE to an equilibrium configuration. After energy minimization, all wires were equilibrated for 200 ps at 300 K using the Nosé-Hoover thermostat together with the Nosé-Hoover barostat [67] applied along the periodic axis to relax possible stresses. The surface states after equilibration at 300 K of the wires with surface roughness or grooves are shown in Fig. S4 in the Supplementary Material. The heights of the resulting surface steps are with 1–2 interatomic distances comparable to the ones observed by high-resolution TEM on the experimentally tested NWs, see Fig. S2 in the Supplementary Material.

Tensile deformation was applied by homogeneously straining the wires and the simulation box along the wire axis at a constant strain rate ($\dot{\epsilon}=2\times10^8~{\rm s}^{-1}$) at 300 K, where the temperature T was controlled with a Nosé-Hoover thermostat. Different strain rates ($\dot{\epsilon}=5\times10^7~{\rm s}^{-1}$, $6\times10^8~{\rm s}^{-1}$ and $1\times10^9~{\rm s}^{-1}$) were also tested. The simulations were

carried out using the MD software package IMD [68]. To identify the defect structures and dislocations, common neighbor analysis (CNA) [69], coordination number and the dislocation extraction algorithm (DXA) [70] as implemented in the atomistic visualization software OVITO [71] were used. The dislocation density was calculated by dividing the total dislocation line length from the DXA output by the initial volume of the NW. The double Thompson tetrahedron notation [72] is employed to describe the dislocation-CTB reactions, see Fig. 1f. All information needed to reproduce the simulation results and the relevant datasets of the stress-strain response and evolution of dislocation density can be found at [73].

3. Results

Building on previous in—situ experiments and MD simulations on SCNWs [12], the aim of this work is to investigate the influence of CTBs on the strength and deformation behavior of NWs.

We first compare the tensile response of MTNWs with previously reported tensile behavior of defect-scarce Au NWs that were grown in identical conditions. For Au SCNWs, two different behaviors have been reported [12,75]. One type shows no significant load drop after yield and fractures after some amount of plasticity without softening. The other category of response shows a large load drop following incipient plasticity, with a subsequent flow regime at a reduced stress. Generally, the latter is ascribed to propagation of a dominant twin along the NW. Despite the large difference in plasticity of SCNWs, the incipient yielding mechanism is shared and hinges on the nucleation of the leading partial dislocation. Selected stress-strain curves of tensile tested SCNWs from Sedlmayr et al. [12] are replotted in Fig. 2a for comparison, Elastic loading of MTNWs follows that of SCNWs although with yield at a higher stress, followed by constant flow stress at the level of the yield stress. Thus, MTNWs maintained high flow stresses (~1.8 GPa) during plastic deformation with final failure occurring at total strains of approximately 5%. We note that this is a remarkable amount of strain that is sustained at very high stresses - in contrast to the quasi-brittle behavior associated with rapid plastic localization. The yield strengths were measured to be 1.81 GPa and 1.84 GPa, significantly higher than the reported mean yield strength of Au SCNWs in tension (1.01 GPa) [74] and outside their scatter band, see Fig. 2d. This suggests a pronounced strengthening effect due to the presence of axial twin boundaries. No dominant deformation twin segments were observed in postmortem TEM micrographs (Fig. 3a); the only remaining residual contrast is attributed to localized bend contours resulting from kink formation. The fractured end shows a relatively flat morphology along the TEM view (Fig. 3b), in contrast to the cone-shaped fracture tip ends of SCNWs (see Fig. S5 in the Supplementary Material). Compared to SCNWs the MTNWs thus show much more strongly spatially localized deformation.

Exemplary stress-strain responses of simulated tensile tests are shown in Fig. 2b for pristine and in Fig. 2c for NWs with a roughness according to the removal of 33% of atoms in the two outermost layers (L2R0.33). The wires with pristine surfaces show only small increases in yield strength when CTBs are present, from 2.01 to 2.06 GPa for the BTNW and to 2.09 GPa for the MTNW, see also Tab. 2 in the Supplementary Material. Introducing surface roughness decreases the yield strengths of the wires to levels comparable to the experiments, see Fig. 2a,c and Fig. 2d. For the SCNWs, the different rough surface states led to a reduction of the yield strength on average by about 23% or 0.4-0.51 GPa, and the introduction of a surface groove reduced the SCNW yield stress by 0.54 GPa, see Tab. 2 in the Supplementary Material. Surface roughness also decreased the yield strength of the TNWs, however to a somewhat lesser degree, see Fig. 2d and Table 2 in the Supplementary Material. When comparing the yield strengths of wires with the same surface state, rough BTNW and MTNW show on average an increase in strength compared to the corresponding SCNW by 3% and 10%, see Fig. 2d. Fig. 2c shows as

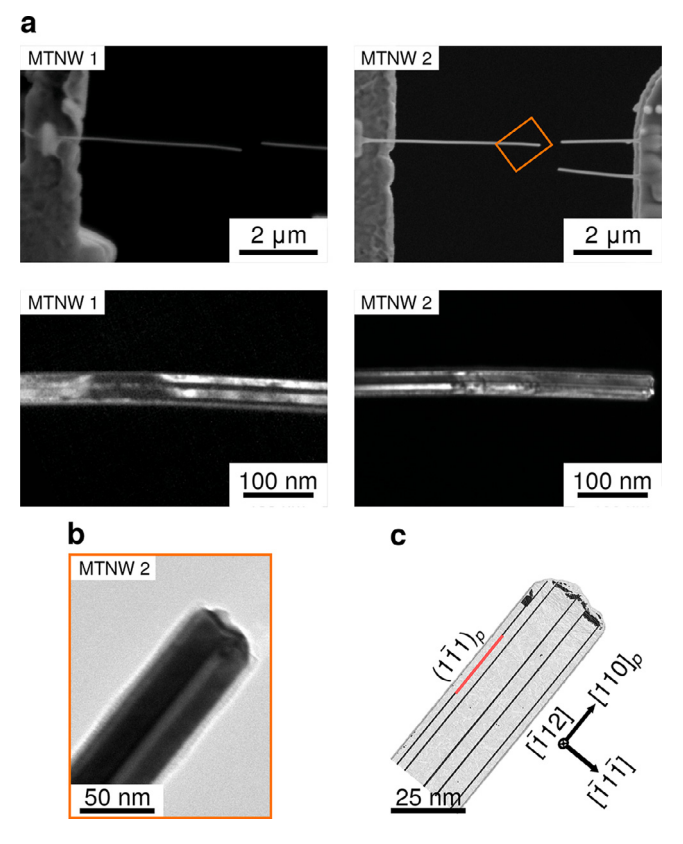


Fig. 3. a SEM (upper) and TEM (lower) images of tensile tested MTNWs showing kinked geometry. **b** TEM image of fractured end of the MTNW. **c** Snapshot from MD simulations showing the fractured end of the MTNW (d=24.5 nm, l=107.3 nm) with L2R0.33 rough surfaces (generated by randomly removing 33% of atoms from the two outermost layers) displaying a jagged surface viewed along [$\overline{1}$ 12] direction. Only outer-layer atoms and atoms that make up the CTB and defects (in black) are shown. Outer-layer atoms are half transparent.

example the stress-strain curves of NWs with surfaces prepared according to the L2R0.33 procedure, where the BTNW and MTNW show a 5% and 15% increase in yield strength, respectively, compared to the SCNW. After the yield point, the wires with pristine surfaces show a more abrupt stress drop than the wires with rough surfaces. The yield strength of the simulated NWs and the experimentally tested SCNWs [74] and MTNWs are summarized in Fig. 2d. A standard t-test on the two experimental data sets (N=27 for SCNW, N=2 for MTNW) calculates t=2.587 and p=0.015. Therefore, adopting the p < 0.05 standard, the difference in the distributions is statistically significant. Clearly, the MTNWs show higher yield strengths than SCNWs in both experiments and MD simulations with any kind of surface defects. The yield strengths of all simulated NWs are in addition listed in Table 2 in the Supplementary Material.

Deformed configurations at identical strains are shown in Fig. 4a—f for NWs with pristine and the L2R0.33 surface states. As additional example, the corresponding configurations for NWs prepared with L4R0.33 surfaces are shown in the Supplementary Material, Fig. S6. The deformation behavior of SCNWs is dominated by deformation twinning, with plastic deformation spread throughout the wires, see, e.g., Fig. 4a,d and S6a. In contrast, TNWs do not show twinning and their deformation is more strongly localized compared to the corresponding SCNWs, see. e.g., Fig. 4b,c and S6b,c. Twinned NWs furthermore show surface steps on the $(1\overline{11})$ and $(\overline{1}11)$ surface facets that have heights of a full Burgers vector projected on the surface facet normals. Few surface steps are observed on $(1\overline{1}1)$ and (001) surface facets except in the region of necking. The bottom view of the BTNWs shows furthermore an interesting symmetric slip pattern (Fig. 4b,e, S6b).

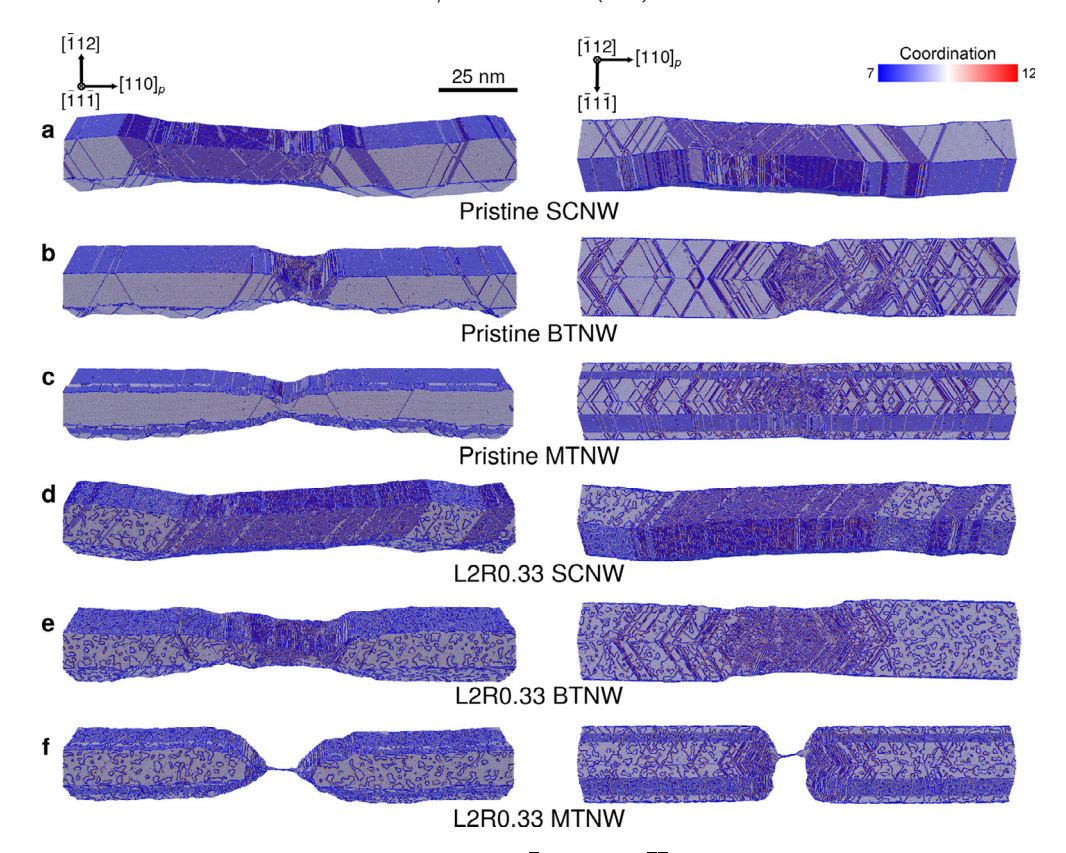


Fig. 4. a-f Configurations at 27.1% strain for the different simulated NWs viewed along $[1\overline{1}1]$ (left) and $[1\overline{1}2]$ (right). L2R0.33 indicates rough surfaces generated by randomly removing 33% of atoms from the two outermost layers. Atoms are colored according to their coordination number.

The trend towards stronger localized deformation in TNWs is even more pronounced for rough TNWs, especially for MTNWs, see Fig. 4 and Fig. S6. Rough MTNWs show furthermore the lowest fracture strains of all tested coresponding NWs, see also Fig. 2c. The fractured end of the MTNW with L2R0.33 surface state shows a flat morphology when viewed along $[\bar{1}12]$ direction (Fig. 3c), in agreement with experimental observations, Fig. 3b. The same is true for the MTNW with L4R0.33 rough surfaces, see Fig. S6c in the Supplementary Material.

The stress-strain curves of NWs of different sizes (Fig. S7), aspect ratios (Fig. S8), and with different applied strain rates (Fig. S9) as well as simulated with different potentials (Fig. S10) can be found in the Supplementary Material. The results of these additional simulations show that the main observations above, namely that CTBs influence the deformation behavior leading to more localized failure and that they can increase the yield strength of NWs, are insensitive to these simulation parameters and the used potentials.

4. Discussion

4.1. Deformation twinning in SCNWs

The deformation behavior under tension of the (110)-oriented FCC SCNWs shown in Fig. 2b,c, Fig. 4a,d and S6 in the Supplementary Material agree well with previous work [8,11–13,15–17,23], providing an important baseline for ascertaining the influence of CTBs.

The occurrence of deformation twinning can be explained by the different resolved shear stresses on leading and trailing partial dislocations [13,23]. Under tension, the Schmid factors for the leading and trailing partial dislocations on the primary slip systems in [110]-oriented NWs are 0.471 and 0.236, respectively. In turn, the leading partial dislocation experiences two times the resolved shear stress of that of the trailing partial dislocation. Therefore, the successive nucleation of a trailing partial dislocation is not favorable. Instead,

the self-stimulated nucleation of leading partial dislocations on adjacent slip planes leads to the growth of deformation twins in these SCNWs [12,13]. Consequently, the same NW under compression shows full dislocation nucleation [8,13,24]. In general, the difference in unstable stacking fault energy, intrinsic stacking fault energy and unstable twinning energy, as well as the change of surface energy in twinned segments need to be taken into account to explain and predict size-dependent twinning in FCC metallic SCNWs [8,17,19,76].

4.2. Interactions between dislocations and coherent twin boundaries

The TNWs show more strongly localized deformation behavior compared with the SCNWs in experiments and MD simulations, and surface steps left behind by full dislocation slip are observed in the MD simulations. Slip by full dislocation as in the MD simulations of TNWs was also observed in experiments in the presence of a CTB [44]. In order to obtain a better understanding of the deformation mechanisms in TNWs, dislocation nucleation and dislocation-CTB interactions were analyzed in detail.

The slip systems in p and t exhibit mirror symmetry and share a CTB plane (Fig. 1f). Among the slip systems of a [110]-oriented NW, the applied tensile loading along the wire axis only provides resolved shear stresses on (c) and (d) planes ((c') and (d') planes). These two slip planes (c) and (d) ((c') and (d')) in one grain are conjugated and intersect along one line of atoms in the $[\overline{1}1\overline{1}]$ direction on (001) surfaces. The symmetry of the slip systems explains the observation of symmetric slip step patterns on the $(1\overline{1}\overline{1})$ surface facets in the BTNWs.

Fig. 5 shows the nucleation of the first leading partial dislocation $C\delta$ and its interaction with the CTB in the pristine TNWs. The first leading partial dislocation always nucleated from the corner of the two {111} surface facets in the studied NW geometries with pristine and rough surface states. This locus of nucleation corresponds to the region of highest resolved shear stress on the primary slip systems

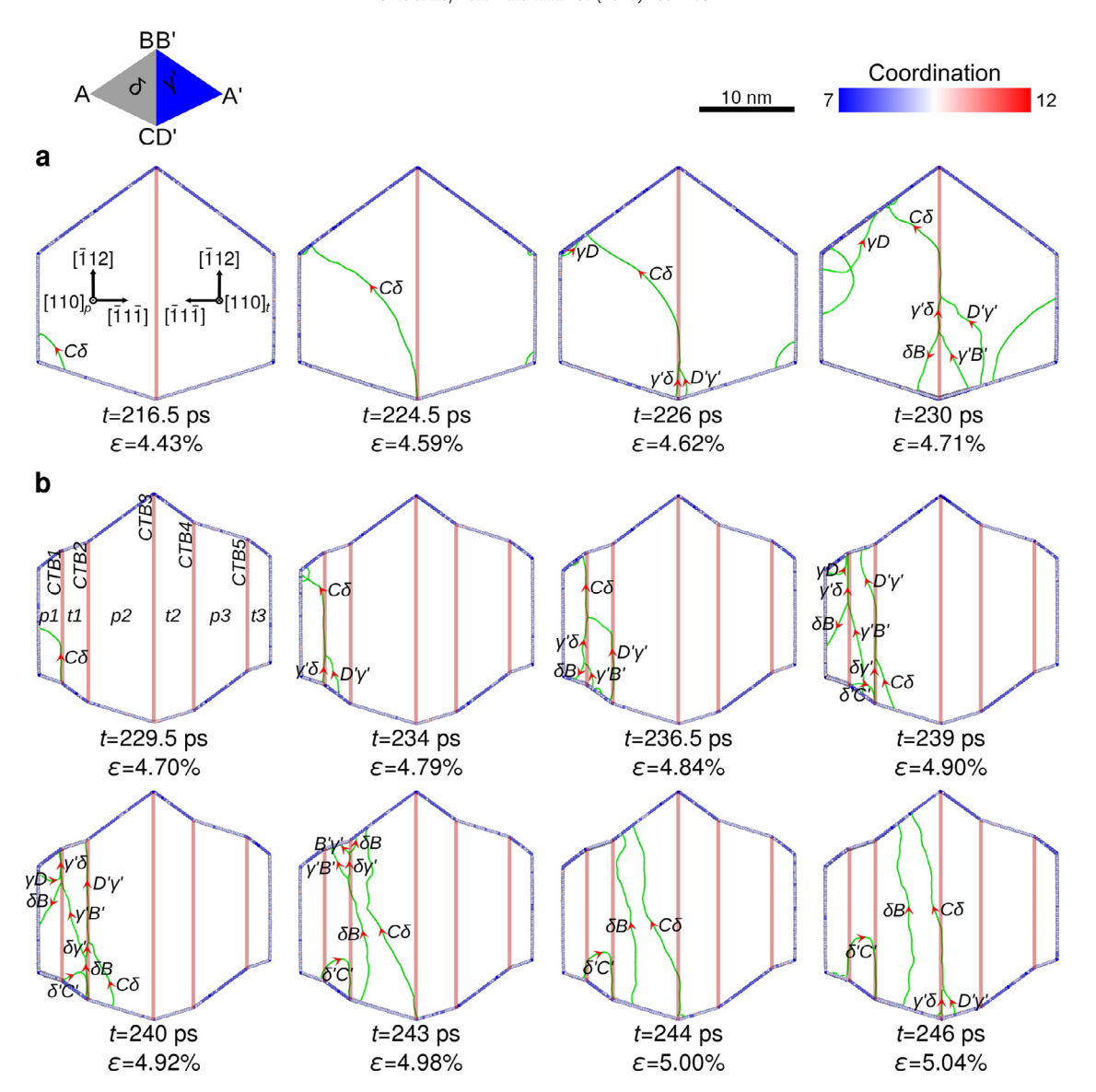


Fig. 5. Dislocation nucleation and dislocation-CTB interactions of the pristine **a** BTNW (d=24.5 nm, l=107.3 nm) and **b** MTNW (d=24.5 nm, l=107.3 nm) during the simulated tensile test (T=300 K, $\dot{\epsilon}=2\times10^8$ s⁻¹). Red half transparent lines indicate the CTBs along the wire axis, red arrows show the direction of dislocation line and the Greek/Roman letters denote the Burgers vector in double Thompson tetrahedron notation. Only outer-layer atoms are shown, that are colored according to their coordination number.

before dislocation emission, see Fig. S11 in the Supplementary Material. For grooved NWs, the first leading partial dislocation $C\delta$ nucleated from the groove instead of the corner, but the dislocation propagated in a similar way as in pristine and rough wires, see Fig. S14 in the Supplementary Material. A surface step with an offset of one partial Burgers vector, which can serve as nucleation site for subsequent dislocations, was left behind on each surface facet after the propagation of the leading partial dislocation. After depositing on the CTB, the leading partial dislocation interacted with the CTB by forming a stair-rod dislocation $\gamma'\delta$. Simultaneously, at the triple junction where the CTB is bounded by two {111} surface facets, a new leading partial dislocation $D'\gamma'$ was stimulated in t on the symmetric slip plane. This reaction can be represented as follows:

$$C\delta \to D'\gamma' + \gamma'\delta$$
. (1)

After the above interaction, the stair-rod dislocation $\gamma'\delta$ dissociated into two trailing partial dislocations δB in p and $\gamma'B'$ in t starting at the intersection of the twin boundary with the surfaces:

$$\gamma'\delta + \delta B \rightarrow \gamma'B',$$
 (2)

which then swept through their respective grains. Eventually, both the leading and trailing partial dislocations escaped at the free surfaces.

Another leading partial dislocation γD on the conjugated slip plane (c) can be stimulated from the surface step on the (001) surface facet left by the first leading partial dislocation $C\delta$. It then interacted with the CTB following similar mechanisms as described in Eq. (1) and (2).

These events repeatedly happened on the same and nearby atomic planes during the deformation processes and lead to a strongly localized deformation behavior in the TNWs. It is important to note, that the observed mechanisms of dislocation nucleation and dislocation-CTB interactions do not change with the surface state (see Fig. S12–14 in the Supplementary Material), sample size (see Fig. S7 in the Supplementary Material), aspect ratio (see Fig. S8 in the Supplementary Material) or used potential (see Fig. S10 in the Supplementary Material). The mechanisms observed here, namely, the transmission of leading partial dislocation and the unzipping of stair-rod dislocation by nucleation of two trailing partial dislocations at the

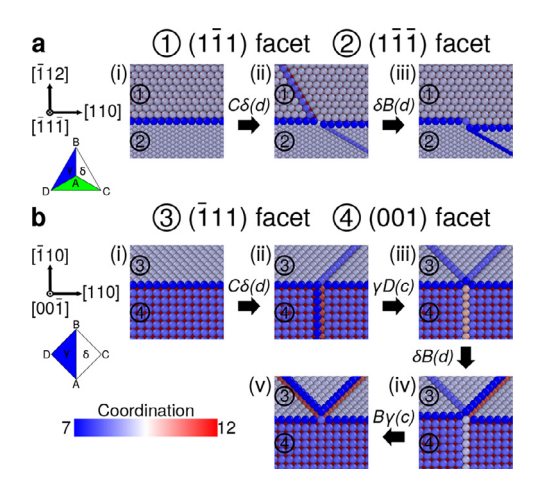


Fig. 6. Schematic illustration of formation and annihilation of surface steps on **a** $(1\overline{1}1)$ and $(1\overline{1}1)$; **b** $(\overline{1}11)$ and (001) surface facets after displacing atoms corresponding to slip by dislocations as observed during tensile tests of TNWs. Atoms are colored according to their coordination number.

intersection of CTB and NW free surfaces, therefore seem to be general and provide an explanation for the observation of full dislocation slip in experiments on Au BTNW [44].

4.3. Formation and annihilation of surface steps

In the deformed TNWs, most surface steps left by dislocation slip are observed on the $(1\overline{11})$ and $(\overline{1}11)$ surface facets. Few are observed on the $(1\overline{1}1)$ and (001) surface facets with the exception of the region of necking. This phenomenon can be explained by the relative orientation between the surface facet normal vectors and the Burgers vectors of the dislocations. Fig. 6 shows examples of the configurations containing $(1\overline{11})$, $(\overline{11})$, (001) and $(\overline{1}1)$ surface facets after displacing atoms corresponding to slip by selected dislocations.

Slip by a leading partial dislocation $C\delta$ produces surface steps with a height of one partial Burgers vector projected on the surface facet normal on the $(1\overline{1}1)$ and $(1\overline{1}\overline{1})$ surface facets (Fig. 6a(i, ii)). The interaction of the leading partial dislocation with the CTB following the mechanisms described by Eqs. (1) and (2) leads to the stimulation of a trailing partial dislocation δB . Slip by this trailing partial dislocation removes the surface step on the $(1\overline{1}1)$ surface facet, and increases the surface step on the $(1\overline{1}1)$ surface facet to a height of one full Burgers vector projected on the surface facet normal (Fig. 6a(ii, iii)).

The (001) surface facet shows a different behavior compared to the other surface facets (Fig. 6b), since two activated conjugated slip planes intersect along one line of atoms in the $[\overline{1}1\overline{1}]$ direction on the (001) surface facet. Slip by a leading partial dislocation $C\delta$ produces surface steps with a height of one partial Burgers vector projected on the surface facet normal on the (001) and $(\overline{1}11)$ surface facets, see Fig. 6b(i, ii). Another leading partial dislocation γD on the conjugated slip plane (c) can be stimulated from the surface step on the (001) surface facet, see Fig. 6b(ii). Slip by the leading partial dislocation γD leads to the step on the (001) surface facet becoming shallower and produces another surface step with a height of one partial Burgers vector projected on the surface facet normal on the $(\overline{1}11)$ surface facet, see Fig. 6b(iii). The interaction of these two leading partial dislocations with the CTB via the mechanisms discussed above leads to the stimulation of two trailing partial dislocations δB and $B\gamma$. Slip by the trailing partial dislocations increases each surface step on the $(\overline{1}11)$ surface facet to a height of one perfect Burgers vector projected on the surface facet normal, and annihilates the surface step on the (001) surface facet (Fig. 6b(iii, iv, v)).

Taken as a whole, the formation and annihilation of surface steps on NW surface facets due to the slip of dislocations fully reconciles the surface-orientation-dependent localization observed in TNWs.

4.4. Strengthening by coherent twin boundaries

The observations from the experiments clearly show that the (110)-oriented MTNWs have significantly higher strengths than

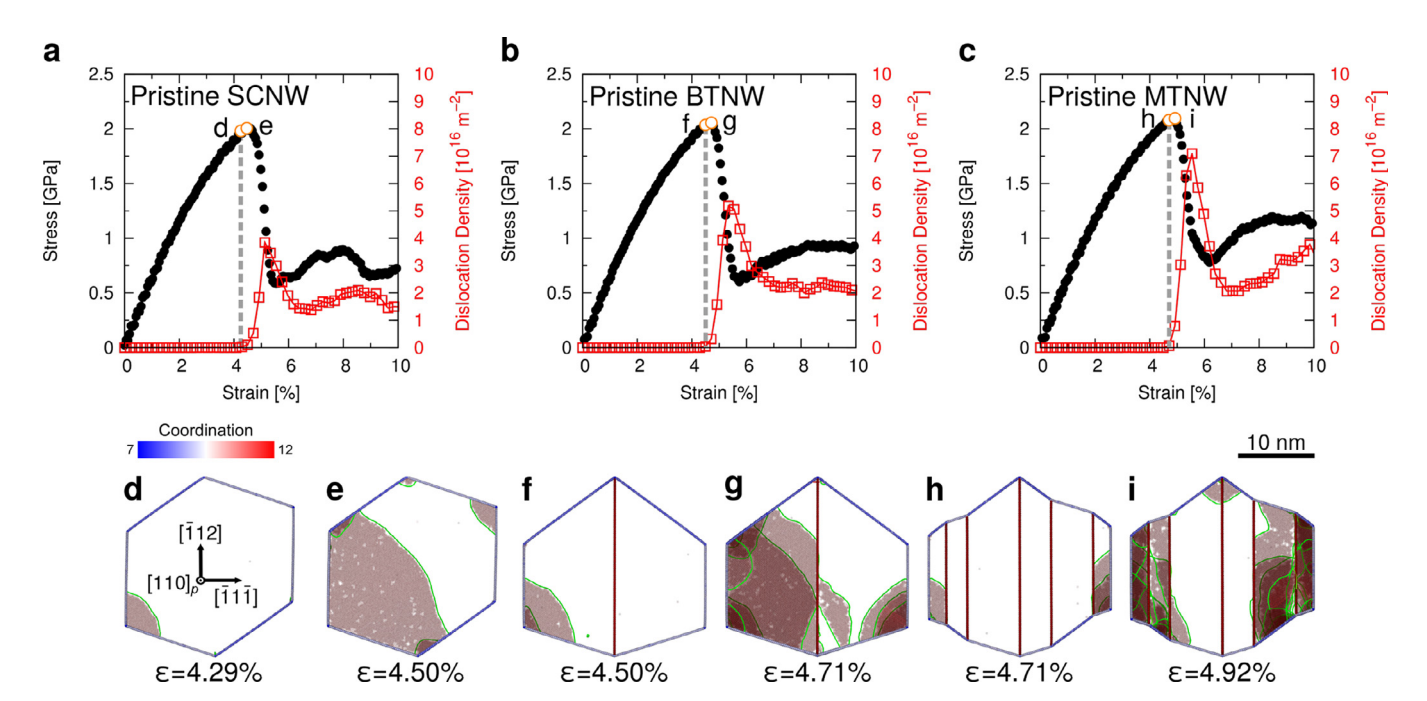


Fig. 7. **a-c** Stress and dislocation density as function of strain in the pristine NWs (d=24.5 nm, l=107.3 nm, T=300 K, $\dot{\epsilon}=2\times10^8$ s⁻¹). Grey dashed lines indicate the stress and strain level when the first dislocation is nucleated. Snapshots of the NWs along [110] viewing direction **d**, **f**, **h** after the nucleation of first dislocation and **e**, **g**, **i** before the initial stress drop. Each snapshot **d**-**i** corresponds to a point labeled in **a-c**. Only outer-layer atoms and atoms belonging to HCP structure are shown here. Atoms belonging to HCP structure are half transparent. Atoms are colored according to their coordination number.

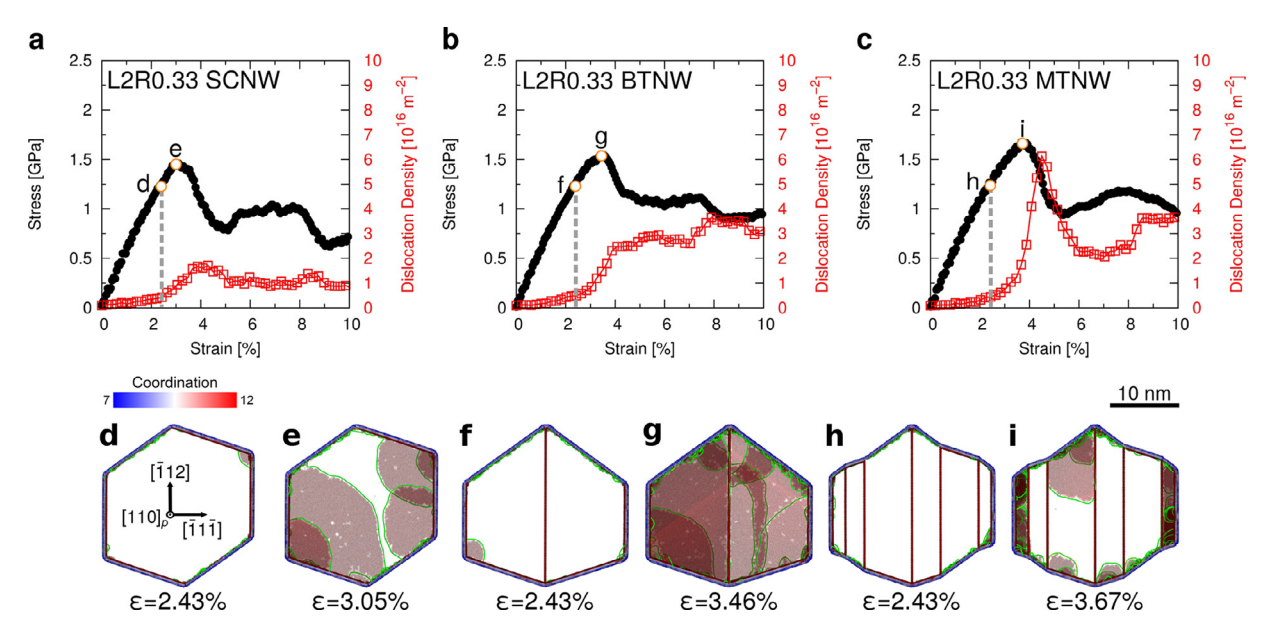


Fig. 8. a-c Stress and dislocation density as function of strain in the NWs with L2R0.33 rough surfaces generated by randomly removing 33% of atoms from the two outermost layers (d=24.5 nm, l=107.3 nm, t=300 K, $\dot{\epsilon}=2\times10^8$ s⁻¹). Grey dashed lines indicate the stress and strain level when the first dislocation is nucleated. Snapshots of the NWs along [110] viewing direction **d, f, h** after the nucleation of first dislocation and **e, g, i** before the initial stress drop. Each snapshot **d-i** corresponds to a point labeled in **a-c**. Color coding is the same as in Fig. 7.

SCNWs of same orientation and similar diameter. In the simulations, NWs with pristine surfaces, however, do not show a strong increase in strength by the presence of CTBs (maximally about 4%). Rough NWs, however, show a more pronounced strengthening by CTBs than pristine NWs, in particular for MTNWs, which show on average an increase in yield strength by around 10% (see Table 2 in the Supplementary Material), and up to 15% in the example shown in Fig. 2c.

To understand this apparently combined effect of CTBs and surface roughness in the simulations, it is important to note that yielding of NWs is not caused by the nucleation of the first (partial) dislocation, but by significant slip of dislocations, either of the initially nucleated one, or of other dislocations. Other dislocations are most often nucleated from sites where the primary dislocation intersected the surface or CTBs, see also [12]. This is clearly evidenced in Figs. 7 and 8, which show the evolution of dislocation density as well as snapshots corresponding to the nucleation of the first partial dislocation and yielding.

Introducing surface roughness or surface grooves lowers the stress to nucleate dislocations, as they cause local stress concentrations [77,78]. The quantitative reduction in critical nucleation stress obviously depends on the exact surface morphology. On average, the different surface states reduce the nucleation stress for the first dislocation in SCNW by 28%, or from 0.45 - 0.72 GPa, see Tab. 3 in the Supplementary Material. For the same surface state (L2R0.33), however, the reduction in nucleation stress is nearly not influenced by the presence of CTBs (by 37% in SCNW, 39% in BTNW and 38% in MTNW), see also Figs. 7 and 8. Note that in all our simulations surface roughness or grooves only influence the nucleation stress, but not the type of defect nucleated or the observed dislocation mechanisms, see Figs. S12-S15 in the Supplementary Material. The type of nucleated defect (here leading partial dislocation or twinning dislocation) is mostly dominated by the resolved shear stress as well as the stacking fault and twin boundary energy.

By lowering the nucleation stress also the resolved shear stress the dislocation is experiencing during a possible interaction with an obstacle is lowered. I.e., when the stress to nucleate a dislocation, e. g., from a pristine surface is higher or comparable to the stress necessary to pass a CTB, the CTB will appear nearly "transparent" to dislocations, and axial CTBs will not appear to provide any strengthening. Only if the stress to nucleate dislocations is lower than the critical

stress for dislocations to pass CTBs, the hardening effect of CTBs becomes obvious. Reducing the stress level in NWs to experimental levels by artificially modifying the surface thus allows to study this hardening effect of CTBs. The simulations are thus in agreement with the experiments and provide an explanation behind the mechanisms for the observed higher yield stress of (110)-oriented Au NWs with axial CTBs.

4.5. The role of surface roughness in atomistic simulations of nanoobjects

In the present study the artificially introduced surface roughness was mainly used as a means to lower the stress level that dislocations are experiencing in a nano-object to more realistic levels, thereby uncovering effects that are not observed at higher stresses. It is, however, important to point out that the roughness in the simulations is comparable to the experimental one, see Fig. S2 in the Supplementary Material.

Furthermore, surface roughness does not only influence the magnitude of the dislocation nucleation stress, but also its distribution. In pristine NWs all geometrically comparable nucleation sites (e.g., corners between {111} surface facets) have identical configuration and therefore require similar stresses to nucleate dislocations. Consequently, the dislocation densities in such pristine wires increases rapidly after the stress to nucleate the first dislocation is reached, as can be seen in Fig. 7. In contrast, the nucleation stresses in a rough wire will follow a broader distribution and after the first dislocation with the lowest nucleation barrier has been emitted, the stress needs to increase to nucleate further dislocations. This is shown to be the case for the NWs with L2R0.33 surface state in Fig. 8, where compared to the pristine NWs fewer dislocations are nucleated after the first nucleation event, and the increase in dislocation density and consequently the stress drop in the rough NWs is less abrupt compared to the case of pristine NWs.

Under typical experimental conditions, even for nano-objects with perfect surfaces, thermal activation will lead to a reduction of the nucleation stress for dislocations and, through its stochastic nature, to scatter or broadening of the distribution of observed nucleation stresses. Artificially introducing surface roughness might thus

also be used to mimic some specific aspects of thermal activation, namely lowering the nucleation stress and a broader distribution of critical stresses. This is important as due to the limitations of MD time scales, simulations at high strain rates can not correctly reproduce the thermally activated nucleation of dislocations in nanoobjects [11]. However, as in the present study, care should be taken to ensure that artificially introduced surface roughness does not alter the nature of nucleated dislocations or the subsequent dislocation processes.

4.6. Transferability of identified mechanisms

Atomistic simulations are severely limited in the size of the samples as well as the time span that can be simulated. Besides the aforementioned problems in directly simulating thermally activated events due to the high strain rates, other effects due to the system size need to be considered. The commonly observed trend in decreasing yield strength with increasing wire diameter in atomistic simulations that is attributed to surface stress effects [8,12,79,80] was also found in our simulations, see Fig. S7 in the Supplementary Material. Similarly, the reported trend in increasingly brittle fracture with increasing wire length in atomistic simulations since the longer wire can store more elastic energy, which in turn drives more localized dislocation activities [81], was also observed in our simulations as well, see Fig. S8 in the Supplementary Material. These effects did, however, not influence the identified mechanisms in dislocation-CTB interactions and their effect on the overall plastic response and failure of NWs. The described interaction mechanisms were also observed in simulations with potentials describing Cu and Ag, see Fig. S10 in the Supplementary Material. It therefore seems plausible, that even though the strain rates, sizes and surface states in the simulations are far from representative for typical experimental conditions, the mechanisms of dislocation-CTB interactions, namely, the transmission of leading partial dislocations and the unzipping of stair-rod dislocations by the nucleation of two trailing partial dislocations at the triple junction where the CTB is bounded by free surfaces, as well as their effect of localizing the plastic deformation in TNWs are also relevant in experimental conditions.

5. Conclusions

In this study, we performed in-situ experiments and MD simulations of tensile tests on (110)-oriented multi-twined nanowires (MTNWs) with coherent twin boundaries (CTBs) parallel to the wire axis. Both, in experiments and simulations, the MTNWs show higher yield stress and enhanced localized deformation compared to single crystalline nanowires (SCNWs). The MD simulations suggest that the mechanisms of dislocation-CTB interactions, namely, the transmission of leading partial dislocations and the unzipping of stairrod dislocations by nucleation of two trailing partial dislocations at the triple junction where the CTB is bounded by free surfaces, provides an explanation for the observation of full dislocation slip. This shows that the intersection of the CTB with free surfaces critically influences the dislocation-CTB interaction and can lead to mechanisms which can not take place in the same way in bulk materials, when CTBs are bounded by grain or interphase boundaries. Slip by full dislocations is repeatedly activated on the same and adjacent atomic planes and therefore leads to a pronounced localization in TNWs. In order to observe the strengthening effect of CTBs, the stress for dislocation nucleation needs to be lower than the stress necessary to activate the identified mechanism of dislocation transmission through the CTB. This is likely the case of experimentally synthesized NWs, even those with nominally high surface quality, and can be achieved in atomistic simulations by artificially introducing surface roughness. With surface roughness, the simulations show comparable levels of yield stresses and strengthening to the

experiments. The simulations furthermore show the importance of the relative orientation between surface facets and the Burgers vector of the activated slip systems, which determines the nature of the occurring surface steps, their potential for nucleating dislocations and subsequently the localization of plastic deformation. Besides providing new mechanistic insights into the strengthening role of CTBs, the results suggests strategies to optimize load-carrying nano-objects, e.g. in nanomechanical systems, by controlling the location of CTBs and surface facets.

Declaration of Competing Interest

The authors declare that they do not have any financial or nonfinancial conflict of interests.

Acknowledgments

We gratefully acknowledge financial support from the German Science Foundation (DFG) via the research training group GRK 1896 "In Situ Microscopy with Electrons, X-rays and Scanning Probes" and the Cluster of Excellence EXC 315 "Engineering of Advanced Materials" (EAM). We also acknowledge support from the National Science Foundation through a CAREER Award #DMR-1056293. Z.X. and E.B. acknowledge financial support from the German Academic Exchange Service (DAAD) via the Programm des Projektbezogenen Personenaustauschs (PPP) Frankreich 2018 (57390426). J.S. and D.S.G. acknowledge support of the A*MIDEX grant (ANR-11-IDEX-0001-02) funded by the French Government "Investissements d'Avenir" program. D.S.G. acknowledges additional support from National Science Foundation (CMMI-1724519). The research reported here made use of shared facilities of the UCSB MRSEC (NSF DMR 1720256), a member of the Materials Research Facilities Network (www.mrfn.org). The authors gratefully acknowledge the compute resources and support provided by the Erlangen Regional Computing Center (RRZE). We furthermore want to thank G. Richter and J. Guénolé for fruitful discussions.

Supplementary material

Supplementary material associated with this article can be found in the online version at doi: 10.1016/j.actamat.2020.01.038

References

- [1] J.-Y. Lee, S.T. Connor, Y. Cui, P. Peumans, Solution-processed metal nanowire mesh transparent electrodes, Nano Lett. 8 (2) (2008) 689–692.
- [2] T. Tokuno, M. Nogi, J. Jiu, K. Suganuma, Hybrid transparent electrodes of silver nanowires and carbon nanotubes: a low-temperature solution process, Nanoscale Res. Lett. 7 (1) (2012) 281.
- [3] F. Guo, H. Azimi, Y. Hou, T. Przybilla, M. Hu, C. Bronnbauer, S. Langner, E. Spiecker, K. Forberich, C.J. Brabec, High-performance semitransparent perovskite solar cells with solution-processed silver nanowires as top electrodes, Nanoscale 7 (5) (2015) 1642–1649.
- [4] B. Wu, A. Heidelberg, J.J. Boland, Mechanical properties of ultrahigh-strength gold nanowires. Nat. Mater. 4 (7) (2005) 525.
- [5] T. Zhu, J. Li, Ultra-strength materials, Prog. Mater. Sci. 55 (7) (2010) 710–757.
- [6] O. Kraft, P.A. Gruber, R. Mönig, D. Weygand, Plasticity in confined dimensions, Annu. Rev. Mater. Res. 40 (2010) 293–317.
- [7] J.R. Greer, J.T.M. De Hosson, Plasticity in small-sized metallic systems: Intrinsic versus extrinsic size effect, Prog. Mater. Sci. 56 (6) (2011) 654–724.
- [8] C.R. Weinberger, W. Cai, Plasticity of metal nanowires, J. Mater. Chem. 22 (8) (2012) 3277–3292.
- [9] Y. Zhu, Mechanics of crystalline nanowires: An experimental perspective, Appl. Mech. Rev. 69 (1) (2017) 010802.
- [10] T.W. Cornelius, O. Thomas, Progress of in situ synchrotron x-ray diffraction studies on the mechanical behavior of materials at small scales, Progr. Mater. Sci. 94 (2018) 384–434.
- [11] L.Y. Chen, M.-r. He, J. Shin, G. Richter, D.S. Gianola, Measuring surface dislocation nucleation in defect-scarce nanostructures, Nat. Mater. 14 (7) (2015) 707.
- [12] A. Sedlmayr, E. Bitzek, D.S. Gianola, G. Richter, R. Mönig, O. Kraft, Existence of two twinning-mediated plastic deformation modes in Au nanowhiskers, Acta Mater. 60 (9) (2012) 3985–3993.

- [13] S. Lee, J. Im, Y. Yoo, E. Bitzek, D. Kiener, G. Richter, B. Kim, S.H. Oh, Reversible cyclic deformation mechanism of gold nanowires by twinning-detwinning transition evidenced from in situ TEM. Nat. Commun. 5 (2014) 3033.
- [14] J. Diao, K. Gall, M.L. Dunn, Surface-stress-induced phase transformation in metal nanowires, Nat. Mater. 2 (10) (2003) 656.
- [15] W. Liang, M. Zhou, Pseudoelasticity of single crystalline Cu nanowires through reversible lattice reorientations, J. Eng. Mater. Tech. 127 (4) (2005) 423–433.
- [16] H.S. Park, K. Gall, J.A. Zimmerman, Shape memory and pseudoelasticity in metal nanowires, Phys. Rev. Lett. 95 (25) (2005) 255504.
- [17] W. Liang, M. Zhou, Atomistic simulations reveal shape memory of FCC metal nanowires, Phys. Rev. B 73 (11) (2006) 115409.
- [18] J. Diao, K. Gall, M.L. Dunn, J.A. Zimmerman, Atomistic simulations of the yielding of gold nanowires, Acta Mater. 54 (3) (2006) 643–653.
- [19] H.S. Park, K. Gall, J.A. Zimmerman, Deformation of FCC nanowires by twinning and slip, J. Mech. Phys. Solids 54 (9) (2006) 1862–1881.
- [20] Y. Zheng, H. Zhang, Z. Chen, L. Wang, Z. Zhang, J. Wang, Formation of two conjoint fivefold deformation twins in copper nanowires with molecular dynamics simulation, Appl. Phys. Lett. 92 (4) (2008) 041913.
- [21] C.R. Weinberger, W. Cai, Orientation-dependent plasticity in metal nanowires under torsion: Twist boundary formation and Eshelby twist, Nano Lett. 10 (1) (2009) 139–142.
- [22] C.R. Weinberger, W. Cai, Plasticity of metal wires in torsion: Molecular dynamics and dislocation dynamics simulations, J. Mech. Phys. Solids 58 (7) (2010) 1011–1025.
- [23] E. Bitzek, Atomistic study of twinning in gold nanowhiskers, J. Solid Mech. Mater. Eng. 6 (1) (2012) 99–105.
- [24] W.G. Nöhring, J.J. Möller, Z. Xie, E. Bitzek, Wedge-shaped twins and pseudoelasticity in FCC metallic nanowires under bending, EML 8 (2016) 140–150.
- [25] Y. Yang, S. Li, X. Ding, J. Sun, E.K. Salje, Interface driven pseudo-elasticity in α-Fe nanowires, Adv. Funct. Mater. 26 (5) (2016) 760–767.
- [26] S. Li, E.K. Salje, S. Jun, X. Ding, Large recovery of six-fold twinned nanowires of α -Fe, Acta Mater. 125 (2017) 296–302.
- [27] L. Lu, Y. Shen, X. Chen, L. Qian, K. Lu, Ultrahigh strength and high electrical conductivity in copper, Science 304 (5669) (2004) 422–426.
- ductivity in copper, Science 304 (5669) (2004) 422–426. [28] K. Lu, L. Lu, S. Suresh, Strengthening materials by engineering coherent internal
- boundaries at the nanoscale, Science 324 (5925) (2009) 349–352. [29] K. Lu, Stabilizing nanostructures in metals using grain and twin boundary architectures, Nat. Rev. Mater. 1 (2016) 16019.
- [30] Z.-H. Jin, P. Gumbsch, E. Ma, K. Albe, K. Lu, H. Hahn, H. Gleiter, The interaction mechanism of screw dislocations with coherent twin boundaries in different face-centred cubic metals, Scripta Mater. 54 (6) (2006) 1163–1168.
- [31] Z.-H. Jin, P. Gumbsch, K. Albe, E. Ma, K. Lu, H. Gleiter, H. Hahn, Interactions between non-screw lattice dislocations and coherent twin boundaries in facecentered cubic metals, Acta Mater. 56 (5) (2008) 1126–1135.
- [32] Y. Zhu, J. Narayan, J. Hirth, S. Mahajan, X. Wu, X. Liao, Formation of single and multiple deformation twins in nanocrystalline fcc metals, Acta Mater. 57 (13) (2009) 3763–3770
- [33] Y. Zhu, X. Wu, X. Liao, J. Narayan, L. Kecskes, S. Mathaudhu, Dislocation—twin interactions in nanocrystalline FCC metals, Acta Mater. 59 (2) (2011) 812–821.
- [34] Y. Zhu, X. Liao, X. Wu, Deformation twinning in nanocrystalline materials, Prog. Mater. Sci. 57 (1) (2012) 1–62.
- [35] B. Wu, A. Heidelberg, J.J. Boland, J.E. Sader, Microstructure-hardened silver, Nano Lett. (2006) 1–5.
- [36] M. Lucas, A.M. Leach, M.T. McDowell, S.E. Hunyadi, K. Gall, C.J. Murphy, E. Riedo, Plastic deformation of pentagonal silver nanowires: Comparison between AFM nanoindentation and atomistic simulations, Phys. Rev. B 77 (24) (2008) 2–5.
- [37] F. Niekiel, E. Bitzek, E. Spiecker, Combining atomistic simulation and X-ray diffraction for the characterization of nanostructures: A case study on fivefold twinned, ACS Nano 8 (2014) 1629–1638.
- [38] Q. Qin, S. Yin, G. Cheng, X. Li, T.H. Chang, G. Richter, Y. Zhu, H. Gao, Recoverable plasticity in penta-twinned metallic nanowires governed by dislocation nucleation and retraction, Nat. Commun. 6 (2015) 5983.
- [39] M. Tian, J. Wang, J. Kurtz, T.E. Mallouk, M. Chan, Electrochemical growth of single-crystal metal nanowires via a two-dimensional nucleation and growth mechanism, Nano Lett. 3 (7) (2003) 919–923.
- [40] J. Wang, M. Tian, T.E. Mallouk, M.H. Chan, Microtwinning in template-synthesized single-crystal metal nanowires, J. Phys. Chem. B 108 (3) (2004) 841–845.
- [41] S. Zhong, T. Koch, M. Wang, T. Scherer, S. Walheim, H. Hahn, T. Schimmel, Nano-scale twinned copper nanowire formation by direct electrodeposition, Small 5 (20) (2009) 2265–2270.
- [42] M. Bernardi, S.N. Raja, S.K. Lim, Nanotwinned gold nanowires obtained by chemical synthesis, Nanotechnology 21 (28) (2010) 285607.
- [43] D. Jang, X. Li, H. Gao, J.R. Greer, Deformation mechanisms in nanotwinned metal nanopillars, Nat. Nanotechnol. 7 (9) (2012) 594–601.
- [44] B. Roos, B. Kapelle, G. Richter, C.A. Volkert, Surface dislocation nucleation controlled deformation of Au nanowires, Appl. Phys. Lett. 105 (20) (2014) 201908.
- [45] A. Kobler, T. Beuth, T. Klöffel, R. Prang, M. Moosmann, T. Scherer, S. Walheim, H. Hahn, C. Kübel, B. Meyer, et al., Nanotwinned silver nanowires: structure and mechanical properties, Acta Mater. 92 (2015) 299–308.
- [46] Y. Zhu, Q. Qin, F. Xu, F. Fan, Y. Ding, T. Zhang, B.J. Wiley, Z.L. Wang, Size effects on elasticity, yielding, and fracture of silver nanowires: In situ experiments, Phys. Rev. B 85 (4) (2012) 1–7.
- [47] T. Filleter, S. Ryu, K. Kang, J. Yin, R.A. Bernal, K. Sohn, S. Li, J. Huang, W. Cai, H.D. Espinosa, Nucleation-controlled distributed plasticity in penta-twinned silver nanowires, Small 8 (19) (2012) 2986–2993.

- [48] A. Cao, Y. Wei, Atomistic simulations of the mechanical behavior of fivefold twinned nanowires, Phys. Rev. B 74 (21) (2006) 1–7.
- [49] A.M. Leach, M. McDowell, K. Gall, Deformation of top-down and bottom-up silver nanowires, Adv. Funct. Mater. 17 (1) (2007) 43–53.
- [50] F. Niekiel, E. Spiecker, E. Bitzek, Influence of anisotropic elasticity on the mechanical properties of fivefold twinned nanowires, J. Mech. Phys. Solids 84 (2015) 358– 379
- [51] A. Cao, Y. Wei, S.X. Mao, Deformation mechanisms of face-centered-cubic metal nanowires with twin boundaries, Appl. Phys. Lett. 90 (15) (2007) 151909.
- [52] K.A. Afanasyev, F. Sansoz, Strengthening in gold nanopillars with nanoscale twins, Nano Lett. 7 (7) (2007) 2056–2062.
- [53] A. Kunz, S. Pathak, J.R. Greer, Size effects in Al nanopillars: Single crystalline vs. bicrystalline, Acta Mater. 59 (11) (2011) 4416–4424.
- [54] Z.X. Wu, Y.W. Zhang, M.H. Jhon, J.R. Greer, D.J. Srolovitz, Nanostructure and surface effects on yield in Cu nanowires, Acta Mater. 61 (6) (2013) 1831–1842.
- [55] G.J. Tucker, Z.H. Aitken, J.R. Greer, C.R. Weinberger, The mechanical behavior and deformation of bicrystalline nanowires, Model. Simul. Mater. Sci. Eng. 21 (1) (2013) 15004.
- [56] B. Xing, S. Yan, W. Jiang, Q.H. Qin, Deformation mechanism of kink-step distorted coherent twin boundaries in copper nanowire, AIMS Mater. Sci. 4 (1) (2017) 102– 117.
- [57] P.J. Imrich, C. Kirchlechner, C. Motz, G. Dehm, Differences in deformation behavior of bicrystalline Cu micropillars containing a twin boundary or a large-angle grain boundary, Acta Mater. 73 (2014) 240–250.
- [58] P.J. Imrich, C. Kirchlechner, D. Kiener, G. Dehm, Internal and external stresses: In situ TEM compression of Cu bicrystals containing a twin boundary, Scripta Mater. 100 (2015) 94–97.
- [59] G. Dehm, B. Jaya, R. Raghavan, C. Kirchlechner, Overview on micro-and nanomechanical testing: New insights in interface plasticity and fracture at small length scales, Acta Mater. 142 (2018) 248–282.
- [60] G. Richter, K. Hillerich, D.S. Gianola, R. Mönig, O. Kraft, C.A. Volkert, Ultrahigh strength single crystalline nanowhiskers grown by physical vapor deposition, Nano Lett. 9 (8) (2009) 3048–3052.
- [61] K.F. Murphy, L.Y. Chen, D.S. Gianola, Effect of organometallic clamp properties on the apparent diversity of tensile response of nanowires, Nanotechnology 24 (23) (2013) 235704.
- [62] D. Magagnosc, G. Kumar, J. Schroers, P. Felfer, J. Cairney, D.S. Gianola, Effect of ion irradiation on tensile ductility, strength and fictive temperature in metallic glass nanowires, Acta Mater. 74 (2014) 165–182.
- [63] H.S. Park, J.A. Zimmerman, Modeling inelasticity and failure in gold nanowires, Phys. Rev. B 72 (5) (2005) 054106.
- [64] Y. Mishin, M. Mehl, D. Papaconstantopoulos, A. Voter, J. Kress, Structural stability and lattice defects in copper: Ab initio, tight-binding, and embedded-atom calculations, Phys. Rev. B 63 (22) (2001) 224106.
- [65] P. Williams, Y. Mishin, J. Hamilton, An embedded-atom potential for the Cu–Ag system, Model. Simul. Mater. Sci. Eng. 14 (5) (2006) 817.
- [66] E. Bitzek, P. Koskinen, F. Gähler, M. Moseler, P. Gumbsch, Structural relaxation made simple, Phys. Rev. Lett. 97 (17) (2006) 170201.
- [67] W.G. Hoover, Canonical dynamics: equilibrium phase-space distributions, Phys. Rev. A 31 (3) (1985) 1695.
- [68] E. Bitzek, F. Gähler, J. Hahn, C. Kohler, G. Krdzalic, J. Roth, C. Rudhart, G. Schaaf, J. Stadler, H.R. Trebin, Recent developments in IMD: Interactions for covalent and metallic systems, in: Proceedings of the High Performance Computing in Science and Engineering 2000, Springer, 2001, pp. 37–47.
- [69] J.D. Honeycutt, H.C. Andersen, Molecular dynamics study of melting and freezing of small lennard-jones clusters, J. Phys. Chem. 91 (19) (1987) 4950–4963.
- [70] A. Stukowski, Structure identification methods for atomistic simulations of crystalline materials, Model. Simul. Mater. Sci. Eng. 20 (4) (2012) 045021.
- [71] A. Stukowski, Visualization and analysis of atomistic simulation data with OVI-TO—the open visualization tool, Model. Simul. Mater. Sci. Eng. 18 (1) (2009) 015012.
- [72] N. Thompson, Dislocation nodes in face-centred cubic lattices, Proc. Phys. Soc. Sect. B 66 (6) (1953) 481.
- [73] E. Bitzek, Z. Xie, MD-simulation-of-twinned-nanowires, 2019. [dataset] Doi:10.22000/237.
- [74] J. Shin, L.Y. Chen, U.T. Sanli, G. Richter, S. Labat, M.-I. Richard, T. Cornelius, O. Thomas, D.S. Gianola, Controlling dislocation nucleation-mediated plasticity in nanostructures via surface modification, Acta Mater. 166 (2019) 572–586.
- [75] J.-H. Seo, H.S. Park, Y. Yoo, T.-Y. Seong, J. Li, J.-P. Ahn, B. Kim, I.S. Choi, Origin of size dependency in coherent-twin-propagation-mediated tensile deformation of noble metal nanowires, Nano Lett. 13 (11) (2013) 5112–5116.
- [76] M. Chen, E. Ma, K.J. Hemker, H. Sheng, Y. Wang, X. Cheng, Deformation twinning in nanocrystalline aluminum, Science 300 (5623) (2003) 1275–1277.
- [77] S. Brochard, P. Beauchamp, J. Grilhé, Stress concentration near a surface step and shear localization, Phys. Rev. B 61 (13) (2000) 8707.
- [78] S. Brochard, P. Hirel, L. Pizzagalli, J. Godet, Elastic limit for surface step dislocation nucleation in face-centered cubic metals: Temperature and step height dependence, Acta Mater. 58 (12) (2010) 4182–4190.
- [79] J. Diao, K. Gall, M.L. Dunn, Yield strength asymmetry in metal nanowires, Nano Lett. 4 (10) (2004) 1863–1867.
- [80] H. Liang, M. Upmanyu, H. Huang, Size-dependent elasticity of nanowires: nonlinear effects, Phys. Rev. B 71 (24) (2005) 241403.
- [81] Z. Wu, Y.-W. Zhang, M.H. Jhon, H. Gao, D.J. Srolovitz, Nanowire failure: long= brittle and short= ductile, Nano Lett. 12 (2) (2012) 910–914.